Template-Free Brain MRI Alignment Using Outlier-Robust Wasserstein Distance under Rigid Transformation

1st Xu Wang
University of Science and Technology of China
Hefei, Anhui, China
worm@mail.ustc.edu.cn

2nd Wenjie Liu
University of Science and Technology of China
Hefei, Anhui, China
lwj1217@mail.ustc.edu.cn

3rd Fuyou Miao
University of Science and Technology of China
Hefei, Anhui, China
mfy@ustc.edu.cn

4th Yan Xiong
University of Science and Technology of China
Hefei, Anhui, China
yxiong@ustc.edu.cn

***Abstract*—Brain MRI alignment is a fundamental topic in neuroscience. However, brain images collected by medical devices are usually noisy, and it is hard to guarantee that all the subjects maintain consistent physical postures during the collection processes; moreover, existing alignment methods often rely on pre-specified templates. To address these challenges, first, we propose a novel alignment method based on *outlier-Robust Wasserstein Distance under Rigid transformation* (RWD). Our method enjoys several advantages, such as it can capture the geometric structure for alignment under rigid transformation, and the outlier robustness can effectively mitigate the impact of noise. Then, we extend our method to compute the corresponding outlier-robust barycenter for group-level analysis. Notably, our approaches for computing pairwise alignments and barycenters are both template-free. Finally, we conduct a set of experiments on brain MRI to evaluate the effectiveness of our alignment method and barycenter algorithm. The results suggest that our approach outperforms the state-of-the-art methods in handling noisy images under rigid transformation.**

***Index Terms*—Outlier-robust Wasserstein distance, Rigid transformation, Brain alignment, Barycenter.**

I. Introduction

Recently, humans have benefited a lot from millimeter anatomical and functional brain imaging. Nevertheless, these images exhibit high variability in anatomo-functional structures [1]. Even for an individual patient, his brain has different structures across different pathological stages [2], [3]. Such variability hinders us from deriving generalizable conclusions from medial images.

To address the variability problem, several alignment methods have been proposed. The popular Multimodal Surface Matching (MSM) [4], [5] aligns functional information after introducing functional maps into the diffeomorphic framework; the heuristics *hyperalignment* [6]–[8] methods align brains by using cortical patches. Additionally, some methods [1], [9], [10] align brains based on Wasserstein distance by modeling brain images as probability measures.

Except for the variability problem, brain images collected by medical devices, such as Functional Magnetic Resonance Imaging (fMRI), are often noisy. As a popular non-invasive imaging technique for recording brain activity, fMRI images are susceptible to various "artifacts" (or "noise"), such as physiological noise [11], motion artifacts [12], and magnetic field inhomogeneity [13]. Furthermore, during image collection processes, it is challenging to guarantee that all subjects maintain consistent physical postures; even the same subject may adopt different postures for different image collection processes. Moreover, existing alignment methods often rely on pre-specified templates; it can be quite challenging if the template is unavailable when studying new species. In conclusion, existing methods [1], [4]–[9] lack robustness to noise and rigid transformations, and often depend on pre-specified templates.

Additionally, individual brains often exhibit substantial deviations in characteristics. To derive generalizable conclusions for a species or group [14]–[17], we often need to compute the barycenter (i.e., average brain) at the group level.

Contributions: To tackle these challenges, **firstly**, we propose an alignment method based on *outlier-Robust Wasserstein Distance [18] under Rigid transformation* (RWD). Our method inherits the ability of Wasserstein distance for capturing geometry structures and thus can capture anatomo-functional structures well, which makes it resilient to local deformations; the outlier robustness mitigates the impact of noise; its invariance under rigid transformation accommodates variations in physical postures across subjects. **Then**, based on our alignment method, we compute the corresponding outlier-robust barycenter for group-level analysis. Notably, our approaches for computing pairwise alignments and barycenters

do not rely on any pre-specified templates[1]. **Finally**, experimental results show that our method can obtain high-quality alignments on noisy datasets; its invariance under rigid transformation frees subjects from maintaining consistent physical postures during the image collection processes. Moreover, the corresponding barycenter algorithm provides finer details for group-level analysis.

II. Preliminaries

A. Notations

Let $[n] := \{1, \ldots, n\}$ and $\|\cdot\|_p$ be the ℓ_p-norm of a vector. Let $(\mathcal{X}, \mathrm{dist})$ be a metric space. Let $\mathbb{R}_+$ be the set of non-negative real numbers. We use $\mathcal{P}(\mathcal{X})$ to denote the probability measure space on $\mathcal{X}$. All rigid transformations in d-dimensional Euclidean spaces $\mathbb{R}^d$ form a mathematical group called Euclidean group $\mathrm{E}(d)$. We denote matrices by capital boldface letters, such as $\mathbf{C}$; C_{ij} is its element in the i-th row and j-th column. Similarly, vectors are represented by lowercase boldface letters, such as $\mathbf{a} := (a_1, \ldots, a_d)^T \in \mathbb{R}^d$; a_i is its i-th element; $\mathbf{a} \succeq \mathbf{b}$ means $a_i \geq b_i$ for all $i \in [d]$. We define $(\mathbf{a}; \mathbf{b}) := (a_1, \ldots, a_d, b_1, \ldots, b_d)^T$ for any $\mathbf{a}, \mathbf{b} \in \mathbb{R}^d$.

Additionally, we define two discrete probability measures

$$\alpha = \sum_{i=1}^{n} a_i \delta_{x_i}, \beta = \sum_{j=1}^{n} b_j \delta_{y_j} \in \mathcal{P}(\mathcal{X}), \tag{1}$$

where $\mathbf{a}, \mathbf{b} \in \mathbb{R}_+^n$ are their weights and $\{x_i\}_{i\in[n]}, \{y_j\}_{j\in[n]} \subseteq \mathcal{X}$ their locations; δ is the Dirac delta function.

The Wasserstein distance [19] is a popular tool for measuring the similarity between two probability measures. However, its sensitivity to noise restricts its applicability in many real-world scenarios; thus, we introduce its robust version to alleviate the impact of outliers.

Definition II.1 (Outlier-robust Wasserstein distance [18])**.** *Given α, β as in (1), $0 \leq \zeta_\alpha, \zeta_\beta < 1, z \geq 1$, and a cost matrix $\mathbf{C} \in \mathbb{R}_+^{n\times n}$ with $C_{ij} = \mathrm{dist}^z(x_i, y_j)$, the outlier-robust Wasserstein distance between α and β is*

$$W(\alpha, \beta) := \min_{\mathbf{P}\in\Pi(\alpha,\beta)} \langle \mathbf{P}, \mathbf{C} \rangle,$$

where $\Pi(\alpha, \beta) = \big\{\mathbf{P} \in \mathbb{R}_+^{n\times n} \;\big|\; \|\mathbf{a}'\|_1 = \zeta_\alpha, \|\mathbf{b}'\|_1 = \zeta_\beta, \mathbf{P}\mathbf{1} = \frac{\mathbf{a}-\mathbf{a}'}{1-\zeta_\alpha}, \mathbf{P}^T\mathbf{1} = \frac{\mathbf{b}-\mathbf{b}'}{1-\zeta_\beta}, \mathbf{a}', \mathbf{b}' \in \mathbb{R}_+^n\big\}$, and $\mathbf{1}$ is the vector of ones.

Remark II.2. *$\mathbf{a}', \mathbf{b}'$ are the weights of outliers for α, β, and $\zeta_\alpha, \zeta_\beta$ are their total mass respectively. The $\Pi(\alpha, \beta)$ is the set of all feasible coupling. In the following, we design our method in a popular metric space, the Euclidean space $\mathbb{R}^d$.*

III. Our Methods

In this section, we first model brain images as probability measures, and then define the RWD for pairwise alignments. Next, we give the algorithm for solving RWD. Further, we compute the corresponding barycenter.

[1]Our method can operate directly on voxels, thus it is template-free. For the template-dependent case, we can fix rigid transformation as identity transformation, which is much simpler than the template-free case.

A. Modeling brains as probability measures

An individual source brain is usually represented by a set of vertexes $\{x_i\}_{i\in[n]} \subseteq \mathbb{R}^d$. Each vertex x_i is associated with both locations (i.e., anatomical information) $\bar{x}_i \in \mathbb{R}^{\bar{d}}$ and features (i.e., functional information) $\hat{x}_i \in \mathbb{R}^{\hat{d}}$ with $d = \bar{d} + \hat{d}$; more specifically, given a pre-specified θ with $0 \leq \theta \leq 1$, we define $x_i = (\theta \cdot \bar{x}_i; (1-\theta) \cdot \hat{x}_i) \in \mathbb{R}^d$, and model the source brain as a measure α as follows

$$\alpha = \sum_{i=1}^{n} a_i \cdot \delta_{(\theta\cdot\bar{x}_i;(1-\theta)\cdot\hat{x}_i)} = \sum_{i=1}^{n} a_i \cdot \delta_{x_i} \in \mathcal{P}(\mathbb{R}^d). \tag{2}$$

Similarly, we define $y_j = (\theta \cdot \bar{y}_j; (1-\theta) \cdot \hat{y}_j) \in \mathbb{R}^d$, and model the target brain as a measure β as follows

$$\beta = \sum_{j=1}^{n} b_j \cdot \delta_{(\theta\cdot\bar{y}_j;(1-\theta)\cdot\hat{y}_j)} = \sum_{j=1}^{n} b_j \cdot \delta_{y_j} \in \mathcal{P}(\mathbb{R}^d). \tag{3}$$

B. Pairwise alignments

For a pre-specified $0 \leq \theta \leq 1$, we define RWD as[2]

$$\mathcal{W}(\alpha, \beta) := \min_{\mathbf{P}\in\Pi(\alpha,\beta), e\in\mathrm{E}(\bar{d})} \theta \cdot \underbrace{\langle \mathbf{P}, e \circ \bar{\mathbf{C}} \rangle}_{\text{term-1}} + (1-\theta) \cdot \underbrace{\langle \mathbf{P}, \widehat{\mathbf{C}} \rangle}_{\text{term-2}} \tag{4}$$

to measure the similarity between α and β, where e is rigid transformation, $\bar{C}_{ij} = \|\bar{x}_i - \bar{y}_j\|_2^2, \widehat{C}_{ij} = \|\hat{x}_i - \hat{y}_j\|_2^2$ and $(e \circ \bar{C})_{ij} = \|e \circ \bar{x}_i - \bar{y}_j\|_2^2$. The coupling $\mathbf{P}$ induced by $\mathcal{W}(\alpha, \beta)$ gives the alignment relationship between the source brain and the target brain. The term-1 maintains the anatomical structures, the term-2 preserves the feature information, and θ makes a trade-off between them.

C. Algorithm for RWD

The aim of Algorithm 1 is to find a measure $\tilde{\alpha} \in \mathcal{P}(\mathcal{X})$ such that $\mathcal{W}(\alpha, \beta) = W(\tilde{\alpha}, \beta)$. We solve $\mathcal{W}(\alpha, \beta)$ by updating the coupling $\mathbf{P}$ and rigid transformation e alternatively. First, we fix e, and have

$$\begin{aligned} \mathcal{W}_e(\alpha, \beta) &:= \min_{\mathbf{P}\in\Pi(\alpha,\beta)} \langle \mathbf{P}, \theta \cdot (e \circ \bar{\mathbf{C}}) + (1-\theta) \cdot \widehat{\mathbf{C}} \rangle \\ &= \min_{\mathbf{P}\in\Pi(\alpha,\beta)} \langle \mathbf{P}, \mathbf{C} \rangle = W(e \circ \alpha, \beta), \end{aligned} \tag{5}$$

where $C_{ij} := \theta \cdot \|e \circ \bar{x}_i - \bar{y}_j\|_2^2 + (1-\theta) \cdot \|\hat{x}_i - \hat{y}_j\|_2^2$ and $e \circ \alpha := \sum_{i=1}^n a_i \cdot \delta_{(\theta\cdot(e\circ\bar{x}_i);(1-\theta)\cdot\hat{x}_i)}$; thus, we can update $\mathbf{P}$ by computing $W(e \circ \alpha, \beta)$. This step can be solved within $\tilde{\mathcal{O}}(\frac{n^2}{\epsilon_+})$ time [20], where ϵ_+ is the pre-specified additive error.

Then, we fix $\mathbf{P}$, and have $\arg\min_e \mathcal{W}_{\mathbf{P}}(\alpha, \beta) = \arg\min_e \langle \mathbf{P}, e \circ \bar{\mathbf{C}} \rangle$. We partition the rigid transformation e into translation transformation e_1 and orthogonal transformation e_2; that is, $e = e_2 \circ e_1$. The translation transformation can be updated as $e_1 = \sum_{i=1}^n \sum_{j=1}^n P_{ij} y_j - \sum_{i=1}^n \sum_{j=1}^n P_{ij} x_i$. For fixed $e_1, \mathbf{P}$, computing the optimal orthogonal transformation e_2 is an orthogonal Procrustes problem [21]. More specifically,

[2]The subscript $*$ in $\mathcal{W}_*(\cdot,\cdot)$ means that we fix the parameter $*$. For example, $\mathbf{P}$ in $\mathcal{W}_{\mathbf{P}}(\cdot,\cdot)$ means that we fix the parameter $\mathbf{P}$.

we first obtain $\mathbf{M} = \sum_{ij} P_{ij} x_i y_j^T$, and apply singular value decomposition $\mathbf{M} = \mathbf{U}\mathbf{D}\mathbf{V}^{\mathbf{T}}$; then, we have

$$e_2 = \mathbf{U}\mathbf{V}^T. \tag{6}$$

Remark III.1. *In our method, the locations of β are fixed, and the rigid transformation is imposed on source α. Moreover, ζ_α means that $\|\mathbf{P}\mathbf{1} - \mathbf{a}\|_1 \leq 2 \cdot \zeta_\alpha$. For the case $\zeta_a = 0, \zeta_b = 0$, $\mathcal{W}(\cdot,\cdot)$ is a (semi-)metric.*

Algorithm 1 Algorithm for alignments

Input: $\alpha, \beta, \zeta_\alpha, \zeta_\beta$

t = 0;
for $t < T_{align}$ **do**
  t = t +1;
  ▷ update coupling $\mathbf{P}$
  Obtain coupling $\mathbf{P}$ by computing $W(e \circ \alpha, \beta)$ according to (5);
  ▷ update translation transformation e_1 and orthogonal transformation e_2
  Compute $e_1 = \sum_{i=1}^n \sum_{j=1}^n P_{ij} y_j - \sum_{i=1}^n \sum_{j=1}^n P_{ij} x_i$;
  Compute $e_2 = \mathbf{U}\mathbf{V}^T$ according to (6), and set $e = e_2 \circ e_1$;
end for

Output: $\mathbf{P}, \tilde{\alpha}$

D. Algorithm for barycenter

Let

$$\begin{aligned} \mathcal{Q} = \{\alpha^k &= \sum_{i=1}^n a_i^k \cdot \delta_{(\theta \cdot \bar{x}_i^k; (1-\theta)\cdot \hat{x}_i^k)} \\ &= \sum_{i=1}^n a_i^k \cdot \delta_{x_i^k} \in \mathcal{P}(\mathbb{R}^d)\}_{k\in[m]} \end{aligned} \tag{7}$$

be a set of m measures with ζ_α being their mass of outliers. The barycenter on $\mathcal{Q}$ is a measure β (as in (3)) with ζ_β being its mass of outliers, and satisfies

$$\beta = \arg \min_{\beta \in \mathcal{P}(\mathbb{R}^d)} \sum_{k=1}^m \mathcal{W}(\alpha^k, \beta). \tag{8}$$

To simplify the algorithm for computing barycenter, we pre-specified the weights and locations of the barycenter. Thus, we only need to optimize its features. In the following, we compute the barycenter β by updating the couplings $\mathbf{P}^k, k \in [m]$ and the features $\{\hat{y}_j\}_{j\in[n]}$ alternatively. More specifically, we first compute the $\mathbf{P}^k, \tilde{\alpha}^k$ with $(\alpha^k, \beta, \zeta_\alpha, \zeta_\beta)$ as input by Algorithm 1, and set $\alpha^k = \tilde{\alpha}^k$. Then, the features of β are computed by

$$\hat{y}_j = \sum_{k=1}^m \sum_{i=1}^n P_{ij}^k \hat{x}_{ij}^k / (\sum_{k=1}^m \sum_{i=1}^n P_{ij}^k). \tag{9}$$

The detailed procedures are in Algorithm 2.

The β_0 can be obtained by selecting the $\alpha \in \mathcal{Q}$ that minimize $\sum_{k=1}^m \mathcal{W}(\alpha^k, \alpha)$. Actually, we can also initialize β_0 by selecting a measure from $\mathcal{Q}$ randomly. If the number n of voxels for the images is large, we can improve the scalability by clustering algorithms. Specifically, we gather the voxels into several clusters, represent each cluster by its center, and assign the size of the cluster as its weight; that is, we replace images with a set of weighted centers.

Algorithm 2 Algorithm for barycenter

Input: $\mathcal{Q} = \{\alpha^k\}_{k\in[m]}, \beta_0, \zeta_\alpha, \zeta_\beta$

t = 0, $\beta = \beta_0$;
for $t < T_{BC}$ **do**
  t = t + 1;
  ▷ update coupling $\mathbf{P}^k$.
  For each $\alpha^k, k \in [m]$, compute $\mathbf{P}^k, \tilde{\alpha}^k$ by Algorithm 1 with $(\alpha^k, \beta, \zeta_\alpha, \zeta_\beta)$ as input;
  Set $\alpha^k = \tilde{\alpha}^k$;
  ▷ update features
  For each $\hat{y}_j, j \in [n]$, compute $\hat{y}_j$ by using (9);
  $\beta = \sum_{j=1}^n b_j \cdot \delta_{(\theta \cdot \bar{y}_j; (1-\theta)\cdot \hat{y}_j)}$;
end for

Output: β

IV. Experiments

This section demonstrates the effectiveness of our method for computing pairwise alignments and barycenter. All experiments are performed on a server equipped with 2.40GHz Intel CPU, NVIDIA GeForce RTX 3090 GPU, 64GB main memory, and Python 3.12. Our RWD is executed on the CPU, while FUGW runs on the GPU. Our implementation utilizes some Python libraries [22]–[24].

Dataset: The Individual Brain Charting (IBC)[3] [25], [26] is a high spatial-resolution, multi-task fMRI dataset. We select 13 subjects from IBC, and 433 fMRI maps for each subject; We call the above data an original dataset $\mathcal{Q}$. To generate a noisy dataset $\mathcal{Q}'$, we add $\zeta = \zeta_\alpha = \zeta_\beta$ mass of artifacts and apply a random rotation to each original image. The proper margin violation is at most 2ζ.

A. Pairwise alignments

Evaluation metrics: (i) $\text{diff}_a := \|\mathbf{P}\mathbf{1} - \mathbf{a}\|_1$ records the deviation of coupling $\mathbf{P}$ from margin $\mathbf{a}$. (ii) $\text{diff}_b := \|\mathbf{P}^T\mathbf{1} - \mathbf{b}\|_1$ records the deviation of coupling $\mathbf{P}$ from margin $\mathbf{b}$. (iii) loss_{align} refers to the average distance between pairwise noisy data.

To demonstrate the performance of our pairwise alignment method, we applied our algorithms to the noisy dataset $\mathcal{Q}'$. Each case involves 13 subjects. Thus, we compute $\frac{13\times12}{2} = 78$ pairwise alignments between the subjects. The recorded values are the average results for these 78 pairwise alignments. The hyperparameter ρ of FUGW[4] controls the robustness to noise.

[3]Its original [25] and extended version [26] includes 12 and 15 subjects, respectively.

[4]Code and additional details for FUGW are available on GitHub: ic-casp2025.

Table I shows that our RWD has better alignment quality than FUGW on noisy datasets, and it is robust to rigid transformations. Moreover, our method does not cause excessive margin violation (i.e., $\text{diff}_a = \text{diff}_b \leq 2\zeta$).

TABLE I: Comparisons of different alignment methods on the noisy datasets. WD is a special case of RWD, where rigid transformation is replaced with identity transformation.

ζ	method	ρ	time(s)	diff_a	diff_b	$\text{loss}_{align}(\downarrow)$
0.1	FUGW	0.50	1627	0.28	0.27	$153.14_{\pm 63.16}$
	FUGW	1	1626	0.21	0.21	$154.91_{\pm 63.65}$
	FUGW	2	1626	0.16	0.16	$157.64_{\pm 62.84}$
	WD	None	328	0.20	0.20	$3.35_{\pm 1.12}$
	RWD	None	1475	0.20	0.20	$\mathbf{2.42}_{\pm 0.50}$
0.2	FUGW	0.13	2020	0.44	0.45	$157.83_{\pm 64.94}$
	FUGW	0.25	2021	0.33	0.34	$154.73_{\pm 67.28}$
	FUGW	0.50	2023	0.26	0.27	$157.49_{\pm 66.87}$
	WD	None	398	0.40	0.40	$2.72_{\pm 1.05}$
	RWD	None	1746	0.40	0.40	$\mathbf{2.01}_{\pm 0.54}$
0.3	FUGW	0.03	2651	0.62	0.64	$204.80_{\pm 94.36}$
	FUGW	0.06	2651	0.58	0.59	$196.32_{\pm 93.91}$
	FUGW	0.13	2652	0.46	0.48	$186.11_{\pm 92.22}$
	WD	None	487	0.59	0.59	$3.84_{\pm 2.39}$
	RWD	None	2152	0.59	0.59	$\mathbf{1.74}_{\pm 0.73}$

TABLE II: Comparisons of different barycenter algorithms on noisy datasets.

ζ	method	ρ	time(s)	diff	$loss(\downarrow)$
0.1	FUGW	20	569	0.24	$67.22_{\pm 26.85}$
	FUGW	24	569	0.20	$67.07_{\pm 27.07}$
	FUGW	28	569	0.17	$67.46_{\pm 26.84}$
	WD	None	125	0.20	$68.37_{\pm 28.54}$
	RWD	None	467	0.20	$\mathbf{8.43}_{\pm 0.17}$
0.2	FUGW	12	640	0.48	$23.80_{\pm 6.01}$
	FUGW	16	640	0.35	$23.58_{\pm 5.72}$
	FUGW	20	642	0.27	$23.45_{\pm 5.84}$
	WD	None	139	0.40	$19.20_{\pm 5.52}$
	RWD	None	502	0.40	$\mathbf{1.10}_{\pm 0.11}$
0.3	FUGW	8	732	0.82	$132.55_{\pm 39.10}$
	FUGW	12	732	0.56	$117.68_{\pm 36.00}$
	FUGW	16	732	0.40	$111.21_{\pm 34.96}$
	WD	None	148	0.60	$94.73_{\pm 32.63}$
	RWD	None	562	0.60	$\mathbf{1.19}_{\pm 0.12}$

B. Barycenter

Evaluation metrics: (i) diff records the average deviation of couplings from the weights of m input data and the barycenter. (ii) $loss$ represents the cost incurred from the barycenter to the clean data.

Table II shows the results of our barycenter algorithm. We select six data from the noisy dataset $\mathcal{Q}'$ as input. We compare our barycenter method (RWD-BC) with its corresponding version without rigid transformation (WD-BC) and the FUGW-based method (FUGW-BC). Table II shows that our RWD-BC yields a higher quality barycenter across varying levels of noise.

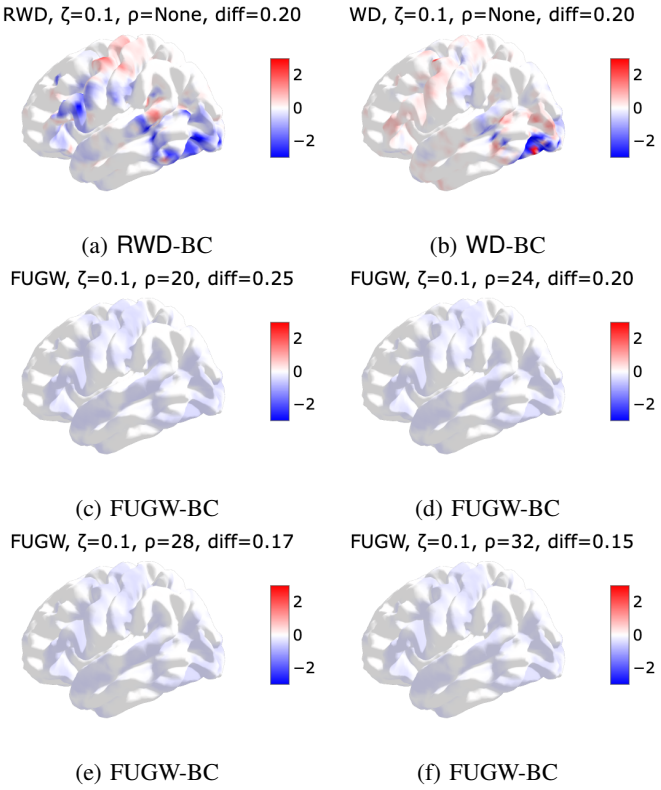

(a) RWD-BC (b) WD-BC (c) FUGW-BC (d) FUGW-BC (e) FUGW-BC (f) FUGW-BC

Fig. 1: z-score of barycenters.

Figure 1 illustrates the z-scores of the barycenters. Compared to FUGW-BC and WD-BC, our RWD-BC captures finer details. The FUGW-BC, which incorporates an entropy regularization term, exhibits a diffusion-like behavior when applied to voxel fMRI images (as seen in Figure 1). In FUGW [1], this diffusion effect is mitigated by mapping voxel images onto a pre-specified template before calculating the barycenter, making the method dependent on pre-specified template. In contrast, our method does not include the entropy regularization term, allowing it to directly handle voxel images without the need for pre-specified templates.

In conclusion, our method achieves better alignment quality and produces a finer barycenter without relying on any pre-specified template. Moreover, it eliminates the need for tuning the parameter ρ to handle varying levels of noise and does not result in excessive marginal violations. Additionally, our algorithm is more computationally efficient on a CPU than FUGW on a GPU, saving both time and hardware resources.

V. Conclusion

This paper proposes an RWD-based alignment method and its corresponding barycenter algorithm. It can tackle outliers efficiently and accommodate variations in physical postures across subjects during image collection. The template-free nature makes it a promising approach, especially for studying new species.

REFERENCES

[1] Alexis Thual, Quang Huy TRAN, Tatiana Zemskova, Nicolas Courty, Rémi Flamary, Stanislas Dehaene, and Bertrand Thirion, "Aligning individual brains with fused unbalanced gromov wasserstein," *Advances in Neural Information Processing Systems*, vol. 35, pp. 21792–21804, 2022.

[2] Arthur W Toga and Paul M Thompson, "Mapping brain asymmetry," *Nature Reviews Neuroscience*, vol. 4, no. 1, pp. 37–48, 2003.

[3] Michael W Weiner, Dallas P Veitch, Paul S Aisen, Laurel A Beckett, Nigel J Cairns, Robert C Green, Danielle Harvey, Clifford R Jack, William Jagust, Enchi Liu, et al., "The alzheimer's disease neuroimaging initiative: a review of papers published since its inception," *Alzheimer's & Dementia*, vol. 9, no. 5, pp. e111–e194, 2013.

[4] Emma C Robinson, Saad Jbabdi, Matthew F Glasser, Jesper Andersson, Gregory C Burgess, Michael P Harms, Stephen M Smith, David C Van Essen, and Mark Jenkinson, "Msm: a new flexible framework for multimodal surface matching," *Neuroimage*, vol. 100, pp. 414–426, 2014.

[5] Matthew F Glasser, Timothy S Coalson, Emma C Robinson, Carl D Hacker, John Harwell, Essa Yacoub, Kamil Ugurbil, Jesper Andersson, Christian F Beckmann, Mark Jenkinson, et al., "A multi-modal parcellation of human cerebral cortex," *Nature*, vol. 536, no. 7615, pp. 171–178, 2016.

[6] James V Haxby, J Swaroop Guntupalli, Andrew C Connolly, Yaroslav O Halchenko, Bryan R Conroy, M Ida Gobbini, Michael Hanke, and Peter J Ramadge, "A common, high-dimensional model of the representational space in human ventral temporal cortex," *Neuron*, vol. 72, no. 2, pp. 404–416, 2011.

[7] J Swaroop Guntupalli, Michael Hanke, Yaroslav O Halchenko, Andrew C Connolly, Peter J Ramadge, and James V Haxby, "A model of representational spaces in human cortex," *Cerebral cortex*, vol. 26, no. 6, pp. 2919–2934, 2016.

[8] Po-Hsuan Cameron Chen, Janice Chen, Yaara Yeshurun, Uri Hasson, James Haxby, and Peter J Ramadge, "A reduced-dimension fmri shared response model," *Advances in neural information processing systems*, vol. 28, 2015.

[9] Alexandre Gramfort, Gabriel Peyré, and Marco Cuturi, "Fast optimal transport averaging of neuroimaging data," in *Information Processing in Medical Imaging: 24th International Conference, IPMI 2015, Sabhal Mor Ostaig, Isle of Skye, UK, June 28-July 3, 2015, Proceedings 24*. Springer, 2015, pp. 261–272.

[10] Thomas Bazeille, Hugo Richard, Hicham Janati, and Bertrand Thirion, "Local optimal transport for functional brain template estimation," in *Information Processing in Medical Imaging: 26th International Conference, IPMI 2019, Hong Kong, China, June 2–7, 2019, Proceedings 26*. Springer, 2019, pp. 237–248.

[11] Gary H Glover, "Overview of functional magnetic resonance imaging," *Neurosurgery Clinics*, vol. 22, no. 2, pp. 133–139, 2011.

[12] Jonathan D Power, Kelly A Barnes, Abraham Z Snyder, Bradley L Schlaggar, and Steven E Petersen, "Spurious but systematic correlations in functional connectivity mri networks arise from subject motion," *Neuroimage*, vol. 59, no. 3, pp. 2142–2154, 2012.

[13] Peter Jezzard and Stuart Clare, "Sources of distortion in functional mri data," *Human brain mapping*, vol. 8, no. 2-3, pp. 80–85, 1999.

[14] Franz-Xaver Neubert, Rogier B Mars, Adam G Thomas, Jerome Sallet, and Matthew FS Rushworth, "Comparison of human ventral frontal cortex areas for cognitive control and language with areas in monkey frontal cortex," *Neuron*, vol. 81, no. 3, pp. 700–713, 2014.

[15] Rogier B Mars, Stamatios N Sotiropoulos, Richard E Passingham, Jerome Sallet, Lennart Verhagen, Alexandre A Khrapitchev, Nicola Sibson, and Saad Jbabdi, "Whole brain comparative anatomy using connectivity blueprints," *Elife*, vol. 7, pp. e35237, 2018.

[16] Ting Xu, Karl-Heinz Nenning, Ernst Schwartz, Seok-Jun Hong, Joshua T Vogelstein, Alexandros Goulas, Damien A Fair, Charles E Schroeder, Daniel S Margulies, Jonny Smallwood, et al., "Cross-species functional alignment reveals evolutionary hierarchy within the connectome," *Neuroimage*, vol. 223, pp. 117346, 2020.

[17] Nicole Eichert, Emma C Robinson, Katherine L Bryant, Saad Jbabdi, Mark Jenkinson, Longchuan Li, Kristine Krug, Kate E Watkins, and Rogier B Mars, "Cross-species cortical alignment identifies different types of anatomical reorganization in the primate temporal lobe," *Elife*, vol. 9, pp. e53232, 2020.

[18] Sloan Nietert, Ziv Goldfeld, and Rachel Cummings, "Outlier-robust optimal transport: Duality, structure, and statistical analysis," in *International Conference on Artificial Intelligence and Statistics*. PMLR, 2022, pp. 11691–11719.

[19] Gabriel Peyré, Marco Cuturi, et al., "Computational optimal transport," *Center for Research in Economics and Statistics Working Papers*, , no. 2017-86, 2017.

[20] Arun Jambulapati, Aaron Sidford, and Kevin Tian, "A direct tilde {O}(1/epsilon) iteration parallel algorithm for optimal transport," *Advances in Neural Information Processing Systems*, vol. 32, 2019.

[21] John C Gower and Garmt B Dijksterhuis, *Procrustes problems*, vol. 30, OUP Oxford, 2004.

[22] Alexandre Abraham, Fabian Pedregosa, Michael Eickenberg, Philippe Gervais, Andreas Mueller, Jean Kossaifi, Alexandre Gramfort, Bertrand Thirion, and Gaël Varoquaux, "Machine learning for neuroimaging with scikit-learn," *Frontiers in neuroinformatics*, vol. 8, pp. 71792, 2014.

[23] Nicolas Bonneel, Michiel Van De Panne, Sylvain Paris, and Wolfgang Heidrich, "Displacement interpolation using lagrangian mass transport," in *Proceedings of the 2011 SIGGRAPH Asia conference*, 2011, pp. 1–12.

[24] Rémi Flamary, Nicolas Courty, Alexandre Gramfort, Mokhtar Z. Alaya, Aurélie Boisbunon, Stanislas Chambon, Laetitia Chapel, Adrien Corenflos, Kilian Fatras, Nemo Fournier, Léo Gautheron, Nathalie T.H. Gayraud, Hicham Janati, Alain Rakotomamonjy, Ievgen Redko, Antoine Rolet, Antony Schutz, Vivien Seguy, Danica J. Sutherland, Romain Tavenard, Alexander Tong, and Titouan Vayer, "Pot: Python optimal transport," *Journal of Machine Learning Research*, vol. 22, no. 78, pp. 1–8, 2021.

[25] Ana Luísa Pinho, Alexis Amadon, Torsten Ruest, Murielle Fabre, Elvis Dohmatob, Isabelle Denghien, Chantal Ginisty, Séverine Becuwe-Desmidt, Séverine Roger, Laurence Laurier, et al., "Individual brain charting, a high-resolution fmri dataset for cognitive mapping," *Scientific data*, vol. 5, no. 1, pp. 1–15, 2018.

[26] Ana Luísa Pinho, Alexis Amadon, Baptiste Gauthier, Nicolas Clairis, André Knops, Sarah Genon, Elvis Dohmatob, Juan Jesús Torre, Chantal Ginisty, Séverine Becuwe-Desmidt, et al., "Individual brain charting dataset extension, second release of high-resolution fmri data for cognitive mapping," *Scientific Data*, vol. 7, no. 1, pp. 353, 2020.

VI. FUGW

Fused Unbalanced Gromov Wasserstein (FUGW) is an approach for aligning pairwise brains based on optimal transformation. We rewrite the Equation (1) of FUGW in [1] as

$$\begin{aligned}\text{FUGW}(\alpha,\beta) :=& \theta \cdot L_W(\mathbf{P}) + (1-\theta)\cdot L_{GW}(\mathbf{P}) + \rho_1 \cdot KL(\mathbf{P}\mathbf{1}|\boldsymbol{\omega}^s) \\ &+ \rho_2 \cdot KL(\mathbf{P}^T\mathbf{1}|\boldsymbol{\omega}^t) + \epsilon \cdot E(\mathbf{P}),\end{aligned} \tag{10}$$

where the term $L_W(\mathbf{P})$ maintains the functional information, the $L_{GW}(\mathbf{P})$ preserves the anatomical structure, and θ makes a trade-off between anatomical structure and functional information; moreover, ρ_1, ρ_2 is used to penalize the margin violations, and $E(\mathbf{P})$ is the entropy regularization term. In our experiments, we set $\rho = \rho_1 = \rho_2$.

Its pairwise alignment between α and β is the coupling $\mathbf{P}$ induced by $\text{FUGW}(\alpha, \beta)$. And its corresponding barycenter on $\{\alpha^k\}_{k\in[m]}$ is a measure β that minimizes the following objective

$$\sum_{k=1}^{m} \text{FUGW}(\alpha^k, \beta). \tag{11}$$

VII. FULL EXPERIMENTS

This section demonstrates the effectiveness of our method for computing pairwise alignments and barycenter. All experiments are performed on a server equipped with 2.40GHz Intel CPU, NVIDIA GeForce RTX 3090 GPU, 64GB main memory, and Python 3.12. Our RWD is executed on the CPU, while FUGW runs on the GPU. Our implementation utilizes some Python libraries [22]–[24].

Dataset: The Individual Brain Charting (IBC)[5] [25], [26] is a high spatial-resolution, multi-task fMRI dataset. We select 13 subjects from IBC, and 433 fMRI maps for each subject; We call the above data an original dataset $\mathcal{Q}$. To generate a noisy dataset $\mathcal{Q}'$, we add $\zeta = \zeta_\alpha = \zeta_\beta$ mass of artifacts and apply a random rotation to each original image. The proper margin violation is at most 2ζ.

A. Pairwise alignments

Evaluation metrics: (i) $\text{diff}_a := \|\mathbf{P}\mathbf{1} - \mathbf{a}\|_1$ records the deviation of coupling $\mathbf{P}$ from margin $\mathbf{a}$. (ii) $\text{diff}_b := \|\mathbf{P}^T\mathbf{1} - \mathbf{b}\|_1$ records the deviation of coupling $\mathbf{P}$ from margin $\mathbf{b}$. (iii) loss_{align} refers to the average distance between pairwise noisy data.

To demonstrate the performance of our pairwise alignment method, we applied our algorithms to the noisy dataset $\mathcal{Q}'$. Each case involves 13 subjects. Thus, we compute $\frac{13\times12}{2} = 78$ pairwise alignments between the subjects. The recorded values are the average results for these 78 pairwise alignments. The hyperparameter ρ of FUGW[6] controls the robustness to noise.

[5]Its original [25] and extended version [26] includes 12 and 15 subjects, respectively.

[6]Code and additional details for FUGW are available on GitHub: iccasp2025.

Table I shows that our RWD has better alignment quality than FUGW on noisy datasets, and it is robust to rigid transformations. Moreover, our method does not cause excessive margin violation (i.e., $\text{diff}_a = \text{diff}_b \leq 2\zeta$).

TABLE III: Comparisons of different alignment methods on noisy dataset. WD is a special case of RWD, where rigid transformation is replaced with identity transformation.

ζ	method	ρ	time(s)	diff_a	diff_b	$\text{loss}_{align}(\downarrow)$
0.1	FUGW	0.02	1626	0.40	0.41	$156.70_{\pm 61.85}$
	FUGW	0.03	1626	0.57	0.55	$150.55_{\pm 59.62}$
	FUGW	0.06	1626	0.59	0.58	$147.28_{\pm 59.99}$
	FUGW	0.13	1616	0.50	0.47	$150.64_{\pm 59.71}$
	FUGW	0.25	1623	0.37	0.37	$151.63_{\pm 61.80}$
	FUGW	0.50	1627	0.28	0.27	$153.14_{\pm 63.16}$
	FUGW	1	1626	0.21	0.21	$154.91_{\pm 63.65}$
	FUGW	2	1626	0.16	0.16	$157.64_{\pm 62.84}$
	WD	None	328	0.20	0.20	$3.35_{\pm 1.12}$
	RWD	None	1475	0.20	0.20	$2.42_{\pm 0.50}$
0.2	FUGW	0.02	2029	0.52	0.47	$172.96_{\pm 67.21}$
	FUGW	0.03	2023	0.60	0.60	$167.30_{\pm 67.81}$
	FUGW	0.06	2021	0.56	0.56	$162.62_{\pm 68.59}$
	FUGW	0.13	2020	0.44	0.45	$157.83_{\pm 64.94}$
	FUGW	0.25	2021	0.33	0.34	$154.73_{\pm 67.28}$
	FUGW	0.50	2023	0.26	0.27	$157.49_{\pm 66.87}$
	FUGW	1	2021	0.20	0.21	$160.16_{\pm 66.20}$
	FUGW	2	2020	0.14	0.16	$159.28_{\pm 66.72}$
	WD	None	398	0.40	0.40	$2.72_{\pm 1.05}$
	RWD	None	1746	0.40	0.40	$2.01_{\pm 0.54}$
0.3	FUGW	0.02	2650	0.52	0.52	$208.50_{\pm 92.33}$
	FUGW	0.03	2651	0.62	0.64	$204.80_{\pm 94.36}$
	FUGW	0.06	2651	0.58	0.59	$196.32_{\pm 93.91}$
	FUGW	0.13	2652	0.46	0.48	$186.11_{\pm 92.22}$
	FUGW	0.25	2652	0.33	0.35	$177.40_{\pm 91.42}$
	FUGW	0.50	2653	0.24	0.27	$173.17_{\pm 91.25}$
	FUGW	1	2651	0.18	0.21	$172.34_{\pm 91.35}$
	FUGW	2	2644	0.13	0.17	$173.02_{\pm 91.79}$
	WD	None	487	0.59	0.59	$3.84_{\pm 2.39}$
	RWD	None	2152	0.59	0.59	$1.74_{\pm 0.73}$

B. Barycenter

Evaluation metrics: (i) diff records the average deviation of couplings from the weights of m input data and the barycenter. (ii) $loss$ represents the cost incurred from the barycenter to the clean data.

Table II shows the results of our barycenter algorithm. We select six data from the noisy dataset $\mathcal{Q}'$ as input. We compare our barycenter method (RWD-BC) with its corresponding version without rigid transformation (WD-BC) and the FUGW-based method (FUGW-BC). Table II shows that our RWD-BC yields a higher quality barycenter across varying levels of noise.

Figures 2 to 4 illustrate the z-scores of the barycenters. Compared to FUGW-BC and WD-BC, our RWD-BC captures finer details. The FUGW-BC, which incorporates an entropy regularization term, exhibits a diffusion-like behavior when applied to voxel fMRI images (as seen in Figure 1). In FUGW [1], this diffusion effect is mitigated by mapping voxel images onto a pre-specified template before calculating the

TABLE IV: Comparisons of different barycenter algorithms on noisy dataset.

ζ	method	ρ	time(s)	diff	$loss(\downarrow)$
0.1	FUGW	4	571	1.11	$66.70_{\pm 26.62}$
	FUGW	8	571	0.64	$67.28_{\pm 26.66}$
	FUGW	12	573	0.42	$67.09_{\pm 26.64}$
	FUGW	16	572	0.31	$67.52_{\pm 26.79}$
	FUGW	20	569	0.24	$67.22_{\pm 26.85}$
	FUGW	24	569	0.20	$67.07_{\pm 27.07}$
	FUGW	28	569	0.17	$67.46_{\pm 26.84}$
	FUGW	32	572	0.15	$67.66_{\pm 26.84}$
	FUGW	36	572	0.14	$67.43_{\pm 27.01}$
	FUGW	40	572	0.12	$67.44_{\pm 26.87}$
	WD	None	125	0.20	$68.37_{\pm 28.54}$
	RWD	None	467	0.20	$8.43_{\pm 0.17}$
0.2	FUGW	4	640	1.18	$24.74_{\pm 5.91}$
	FUGW	8	640	0.73	$24.72_{\pm 5.98}$
	FUGW	12	640	0.48	$23.80_{\pm 6.01}$
	FUGW	16	640	0.35	$23.58_{\pm 5.72}$
	FUGW	20	642	0.27	$23.45_{\pm 5.84}$
	FUGW	24	641	0.22	$23.61_{\pm 5.94}$
	FUGW	28	641	0.19	$23.55_{\pm 5.79}$
	FUGW	32	642	0.16	$23.59_{\pm 6.03}$
	FUGW	36	641	0.15	$23.71_{\pm 5.90}$
	FUGW	40	640	0.13	$23.90_{\pm 5.95}$
	WD	None	139	0.40	$19.20_{\pm 5.52}$
	RWD	None	502	0.40	$1.10_{\pm 0.11}$
0.3	FUGW	4	731	1.12	$160.09_{\pm 43.12}$
	FUGW	8	732	0.82	$132.55_{\pm 39.10}$
	FUGW	12	732	0.56	$117.68_{\pm 36.00}$
	FUGW	16	732	0.40	$111.21_{\pm 34.96}$
	FUGW	20	732	0.31	$108.37_{\pm 34.58}$
	FUGW	24	731	0.25	$107.41_{\pm 34.69}$
	FUGW	28	732	0.21	$106.96_{\pm 34.41}$
	FUGW	32	730	0.18	$106.39_{\pm 34.50}$
	FUGW	36	731	0.16	$105.28_{\pm 34.50}$
	FUGW	40	732	0.14	$105.26_{\pm 34.40}$
	WD	None	148	0.60	$94.73_{\pm 32.63}$
	RWD	None	562	0.60	$1.19_{\pm 0.12}$

barycenter, making the method dependent on pre-specified template. In contrast, our method does not include the entropy regularization term, allowing it to directly handle voxel images without the need for pre-specified templates.

In conclusion, our method achieves better alignment quality and produces a finer barycenter without relying on any pre-specified template. Moreover, it eliminates the need for tuning the parameter ρ to handle varying levels of noise and does not result in excessive marginal violations. Additionally, our algorithm is more computationally efficient on a CPU than FUGW on a GPU, saving both time and hardware resources.

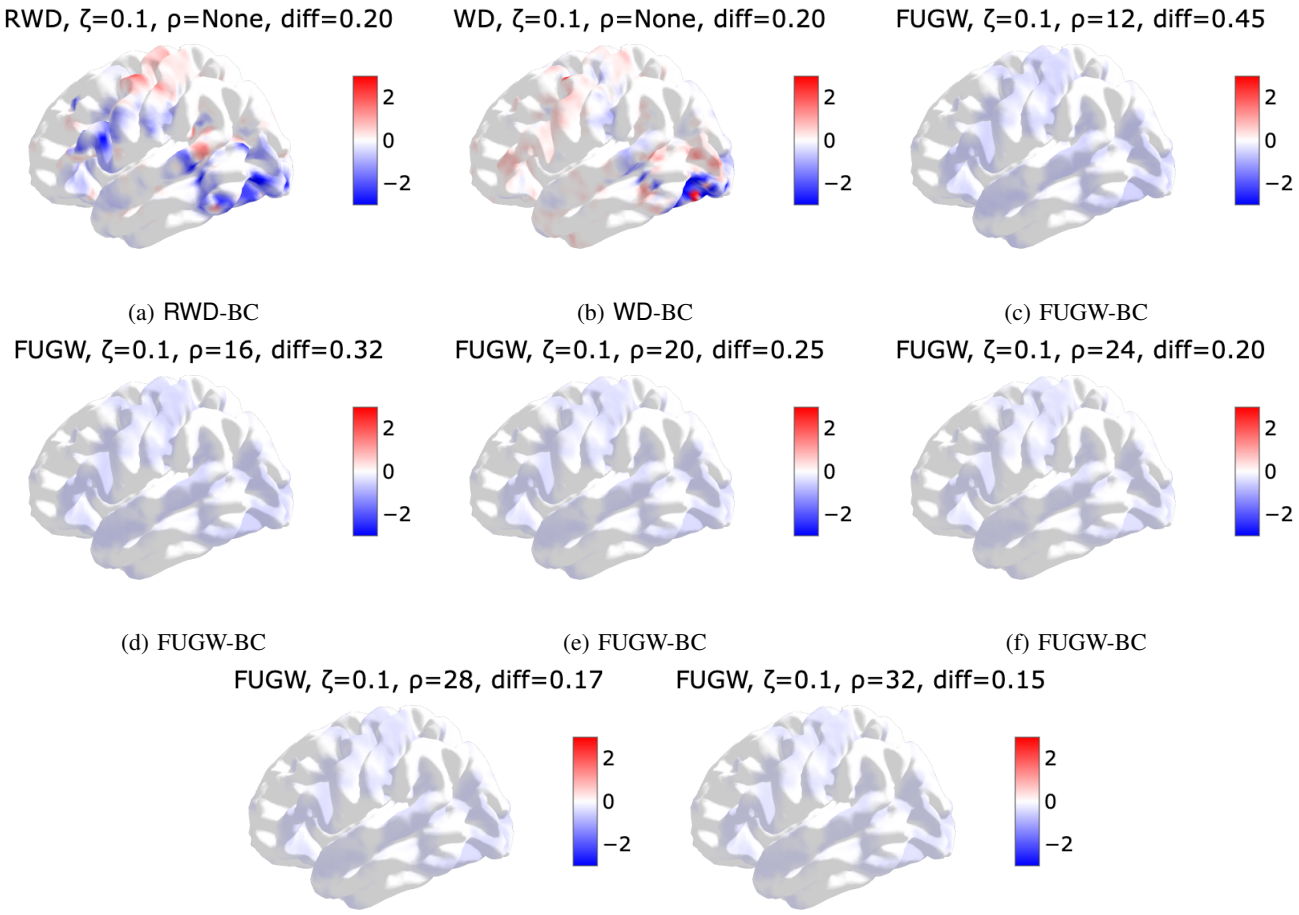

(a) RWD-BC (b) WD-BC (c) FUGW-BC

(d) FUGW-BC (e) FUGW-BC (f) FUGW-BC

(g) FUGW-BC (h) FUGW-BC

Fig. 2: z-score of barycenters with $\zeta = 0.1$.

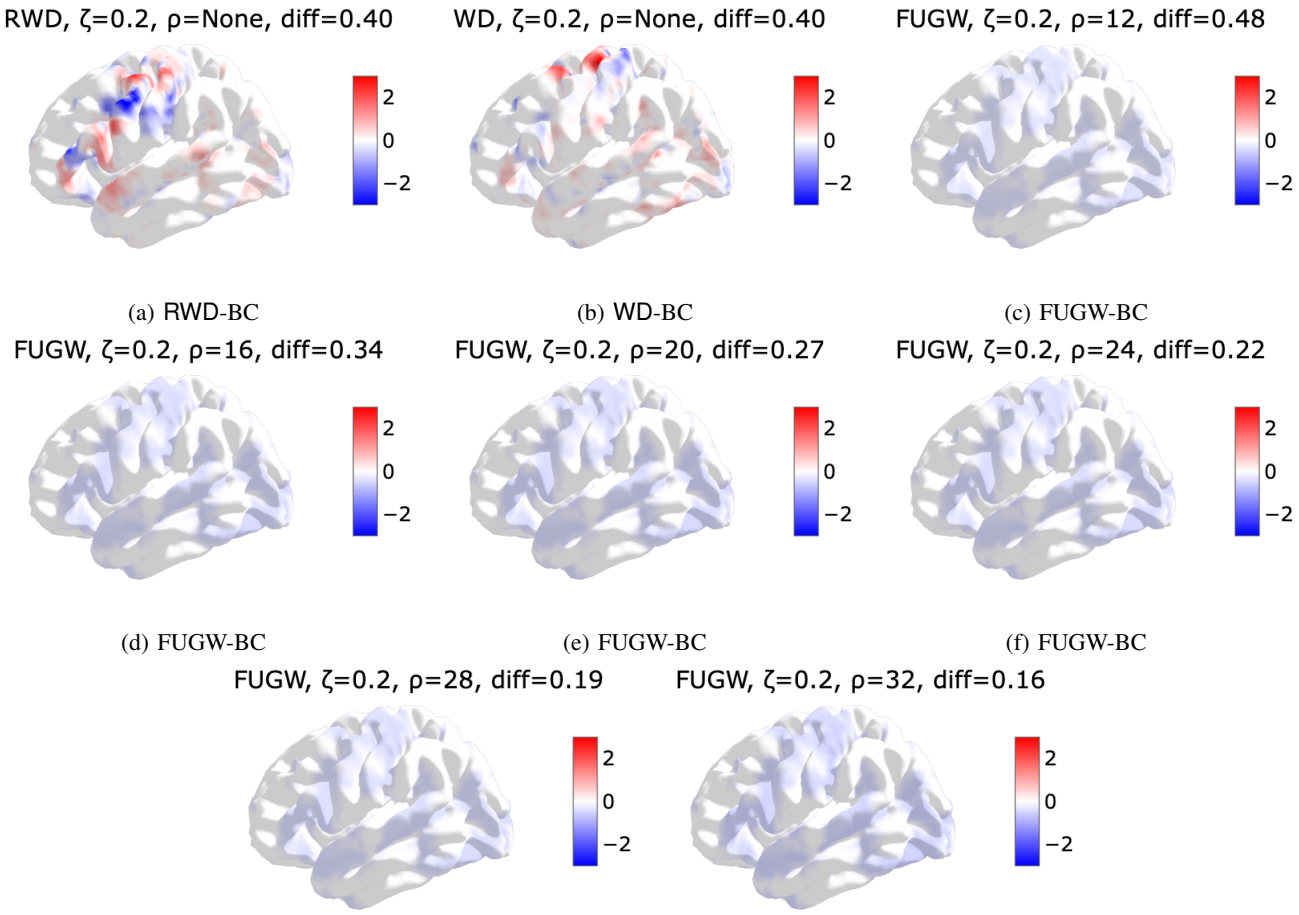

(a) RWD-BC (b) WD-BC (c) FUGW-BC

(d) FUGW-BC (e) FUGW-BC (f) FUGW-BC

(g) FUGW-BC (h) FUGW-BC

Fig. 3: z-score of barycenters $\zeta = 0.2$.

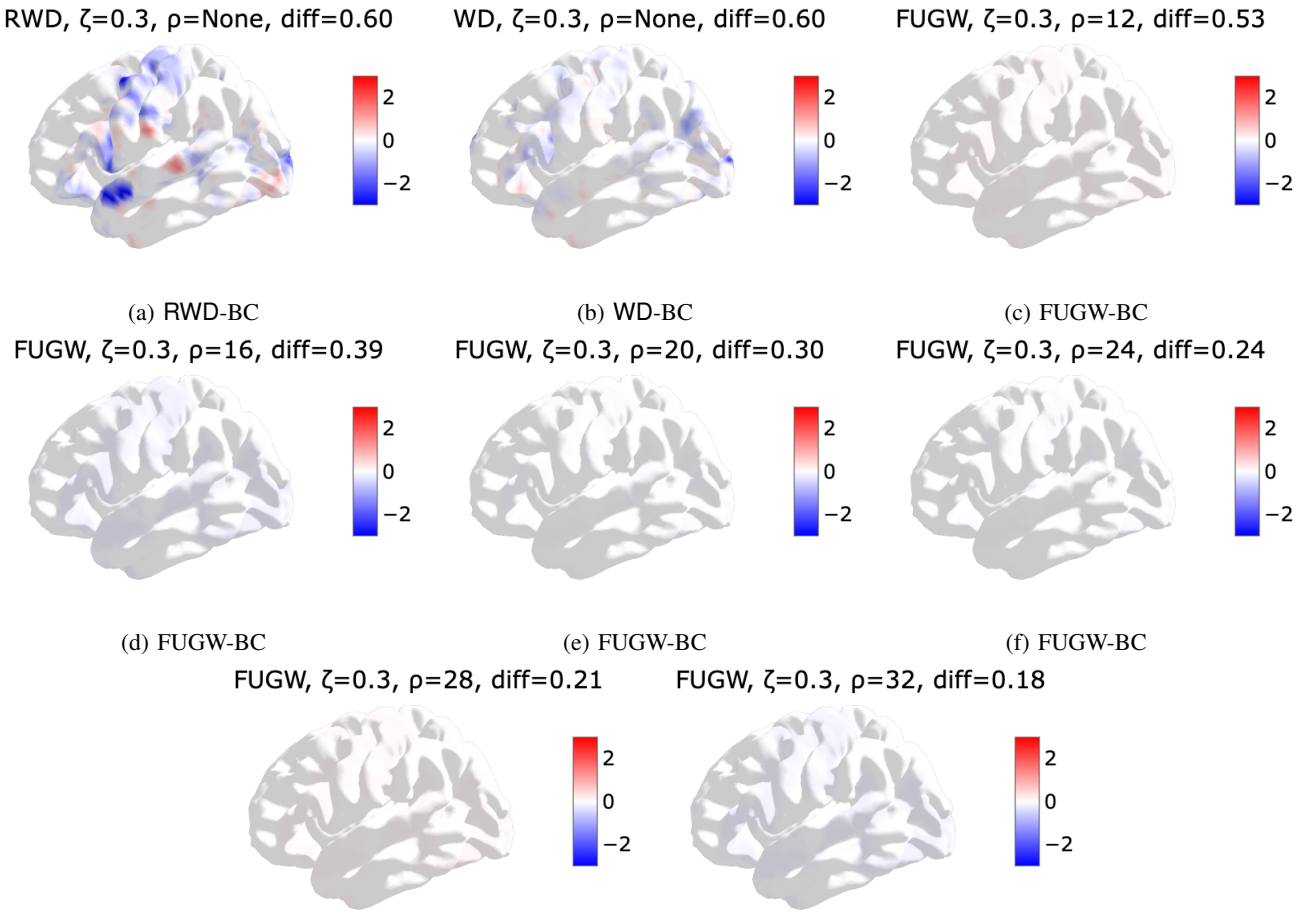

(a) RWD-BC (b) WD-BC (c) FUGW-BC

(d) FUGW-BC (e) FUGW-BC (f) FUGW-BC

(g) FUGW-BC (h) FUGW-BC

Fig. 4: z-score of barycenters $\zeta = 0.3$.